ELECTROCHEMISTRY

# Quantitatively analyzing the failure processes of rechargeable Li metal batteries

**Yuxuan Xiang[1], Mingming Tao[1], Guiming Zhong[2], Ziteng Liang[1], Guorui Zheng[1], Xiao Huang[1], Xiangsi Liu[1], Yanting Jin[3], Ningbo Xu[1], Michel Armand[4], Ji-Guang Zhang[5], Kang Xu[6], Riqiang Fu[7], Yong Yang[1]***



**Practical use of lithium (Li) metal for high–energy density lithium metal batteries has been prevented by the continuous formation of Li dendrites, electrochemically isolated Li metal, and the irreversible formation of solid electrolyte interphases (SEIs). Differentiating and quantifying these inactive Li species are key to understand the failure mode. Here, using operando nuclear magnetic resonance (NMR) spectroscopy together with ex situ titration gas chromatography (TGC) and mass spectrometry titration (MST) techniques, we established a solid foundation for quantifying the evolution of dead Li metal and SEI separately. The existence of LiH is identified, which causes deviation in the quantification results of dead Li metal obtained by these three techniques. The formation of inactive Li under various operating conditions has been studied quantitatively, which revealed a general "two-stage" failure process for the Li metal. The combined techniques presented here establish a benchmark to unravel the complex failure mechanism of Li metal.**

## INTRODUCTION

Li-ion battery (LiB) has significantly redefined the ways we communicate, transport, and reside. However, the increasing demand for high–energy density storage devices in the ever-growing 5G era presents great challenges that now LiBs can no longer address, motivating extensive research on the next-generation energy storage materials and chemistries, such as Li metal batteries (LMBs) that include Li||Ni-rich NMC($LiNi_xMn_yCo_{1-x-y}O_2$), Li-oxygen, Li-sulfur, and solid-state Li batteries. The development of all these devices hinges on the successful application of lithium metal anode, which promises the highest gravimetric/volumetric energy density among the known anode materials (*1*), but suffers from parasitic reactions as evidenced by unsatisfactory Coulombic efficiency (CE) and safety hazard linked to Li dendrites (*2*, *3*).

To extend the cycle life of LMBs, many strategies have been proposed, including electrolyte optimization (*4*), current collector modifications (*5*), and the introduction of an artificial solid electrolyte interphase (SEI) (*6*). Nevertheless, the exact failure mechanism of LMBs remains elusive, as often one cannot rationalize why certain strategies work well while others do not. Moreover, the typical CE of lithium metal anode remains far from 99.99%, which is critical in ensuring a long cycle life comparable to LIBs. Current understanding of lithium metal anode has been restricted by the absence of effective characterization techniques, especially techniques that can accurately distinguish and quantify the various forms of inactive Li microstructures under operando conditions.

The Li consumption mainly comes from two sources: (i) chemical instability between Li metal and electrolytes, which leads to the formation of SEI species where Li exists as an ion, and (ii) physical/mechanical instability isolates the dendritic Li metal from the Li metal bulk or current collector during stripping process and results in the formation of dead Li metal in elemental valence ($Li^0$) (*2*). These two processes happen sequentially or in parallel. Moreover, their relative ratio changes dynamically during cycling and are largely affected by operating conditions, such as electrolyte formulations and cycle protocols, which may be governed by entirely different failure mechanisms, leading to conflicting conclusions depending on which characterizing methods are used or at which stage the analysis is applied.

Quantitative analysis of the dead Li metal and SEI is made difficult by their confusable morphologies and their moisture sensitivity, which challenges most analytic techniques. Fang *et al.* (*7*) developed an elegant quantitative ex situ technique—titration gas chromatography (TGC) to quantify the dead lithium metal and $Li^+$-containing SEI species, and identified the former as the culprit of inactive lithium during the initial cycles. A separate study combining $^7$Li nuclear magnetic resonance (NMR) spectroscopy with TGC was then reported to quantify dead Li metal and SEI when plating and stripping Li on a copper current collector (*8*). However, it is challenging for such a postmortem (hence destructive) analysis to monitor the dynamic evolution process of dead Li metal during electrochemical cycling or under operando conditions.

Recently, Grey and co-workers used in situ NMR spectroscopy to quantify the dead Li metal and SEI in the Cu||$LiFePO_4$ [anode-free batteries (AFBs)] cells for the initial five cycles (*9*). They observed that the formation of SEI is more notable than that of dead Li metal for all electrolytes they studied, with this result contradicting the previous TGC results (*7*, *9*). These inconsistent conclusions suggest that accurately quantifying the dead Li from a single technique is difficult. Therefore, mutual verification or independent reference is urgently required to establish the benchmark

[1]State Key Laboratory for Physical Chemistry of Solid Surfaces, Collaborative Innovation Center of Chemistry for Energy Materials and Department of Chemistry, College of Chemistry and Chemical Engineering, Xiamen University, Xiamen 361005, China. [2]Laboratory of Advanced Spectro-electrochemistry and Li-ion Batteries, Dalian Institute of Chemical Physics, Chinese Academy of Sciences, Dalian 116023, China. [3]Department of Chemistry, University of Cambridge, Lensfield Road, Cambridge CB2 1EW, UK. [4]Basque Research and Technology Alliance (BRTA), Álava Technology Park, Albert Einstein 48, 01510 Vitoria-Gasteiz, Spain. [5]Energy and Environment Directorate, Pacific Northwest National Laboratory, Richland, WA 99354, USA. [6]Battery Science Branch, Energy and Biotechnology Division, Sensor and Electron Devices Directorate, US Army Research Laboratory, Adelphi, MD 20783, USA. [7]National High Magnetic Field Laboratory, 1800 E. Paul Dirac Drive, Tallahassee, FL 32310, USA.
*Corresponding author. Email: yyang@xmu.edu.cn

of quantitative techniques for reliable quantitative results. While previous work only focused on the initial stage of cycling, an analysis of the failure mechanism under prolonged cycles is key to pursue the long cycle life of LMBs (*7*, *9*). It is well documented that the CE of LMBs would drop/fluctuate during prolonged cycles (*3*). Therefore, it is reasonable to speculate that the battery failure mechanism under prolonged cycles would be different from the initial state. Without clarifying the failure mechanism during the whole cycle life of batteries, reasonably designed LMBs with prolonged cycle life are difficult to achieve.

In this work, we first establish operando NMR setup independently to observe the dynamic deposition and dissolution processes of lithium metal during prolonged cycling and quantified the amount of SEI and dead Li metal by $^7$Li NMR spectra. The feasibility and reliability of the quantitative NMR are then further verified by two independent analytic techniques: TGC and mass spectrometry titration (MST). The difference between these three techniques in quantifying dead Li metal is found to be caused by the presence of LiH. With a more reliable quantification methodology, we studied the failure mechanisms of AFBs under several typical conditions, including the current density, electrolyte additives, and salt concentration. On the basis of these quantitative results, we report a two-stage failure process for AFBs and propose future solutions to mitigate the formation of dead Li.

## RESULTS

### The vanishing Li

The chemical shifts of $^7$Li NMR allow us to differentiate metallic Li metal (~270 ppm) from diamagnetic Li species in the SEI (~0 ppm), as illustrated in fig. S2. The $^7$Li NMR signals of SEI overlap severely with that of electrolyte, making it difficult to be deconvoluted and quantified (*10*, *11*). Hence, we only focus on the $^7$Li NMR signal of the Li metal for later analysis. Figure 1 shows the schematic of operando NMR setup and the corresponding NMR results during the first cycle. During charge of Cu||$LiFePO_4$ cell, lithium ions ($Li^+$) are reduced to metallic Li and deposited on the Cu substrate; during discharge, deposited Li metal is oxidized to $Li^+$ ions with some Li disconnected from the bulk Li metal or current collector and become dead Li metal (Fig. 1B). This deposition/stripping process is tracked by operando NMR (Fig. 1, D and E). Upon charge, the increasing $^7$Li NMR signal around 270 ppm corresponds to the continuous deposition of the lithium metal on the Cu substrate, whereas the decreasing signal upon discharge reflects the stripping process. At the end of discharge, the remaining Li metal signal around 270 ppm is attributed to the dead Li metal (Fig. 1E, green line).

We calculate the capacity loss due to the formation of dead Li metal ($C_{dead}$) and SEI ($C_{SEI}$) on the basis of the analysis of the $^7$Li NMR integral and the electrochemistry data. The method is explained in detail in text S1. The total irreversible capacity ($C_{Ir}$) can be obtained from the electrochemical data as follows

$$C_{Ir}(\text{electrochemistry measured}) = \text{charge capacity} - \text{discharge capacity} \quad (1)$$

Here, we assume that the $C_{Ir}$ originates from the dead Li metal and SEI (*7*). Thus, the capacity loss due to the formation of SEI ($C_{SEI}$) can be calculated by Eq. 2

$$C_{SEI} = C_{Ir}(\text{electrochemistry measured}) - C_{dead}(\text{NMR measured}) \quad (2)$$

According to Eqs. 1 and 2, $C_{dead}$ and $C_{SEI}$ can be quantified separately.

We first use the baseline electrolyte consisting of 1 M $LiPF_6$ in ethylene carbonate (EC)/ethyl methyl carbonate (EMC), in which the diameter of deposited Li metal microstructures is about 2 to 3 μm in our cases (fig. S3A), which is much smaller than the NMR skin depth of Li metal (10.4 μm) at 9.7 T.

Figure 1D shows the evolution of Li metal signals in Cu||$LiFePO_4$ cell in baseline electrolyte during the first cycle, which was cycled between 2.8 and 3.8 V at a current density of 0.5 mA cm$^{-2}$. The selected spectra at 3.8 and 2.8 V represent the signal of total deposited Li metal and the dead Li metal, respectively (Fig. 1F). According to our conversion method, this dead Li metal signal (Fig. 1F) corresponds to 15-μA·hour capacity loss (details shown in text S1). The total irreversible capacity measured by electrochemistry is 27 μA·hour (fig. S4). Therefore, the difference of 12 μA·hour corresponds to the capacity loss caused by the formation of SEI. These capacities are then normalized by the first charge capacity (Table 1), where we conclude that the total irreversible capacity loss in the first cycle is 9.4%, from which 5.2% results from the formation of the dead Li metal and 4.2% due to the formation of SEI layer.

Operando NMR was also performed on cells with extensive cycling, and the amount of dead lithium metal and SEI formed directly determines the cycle life of LMBs. Figure 2 exhibits the charge and discharge profiles and their corresponding signals of Li metal for the whole cycling process, which spans from the first cycle to the complete cell failure (with capacity decays to 0). The evolution of dead Li metal can be directly observed in a qualitative manner (Fig. 2B, red dot line), and its trend appears to be a two-stage process. In the first three cycles, the signal of dead Li metal increases slowly. After that, the dead Li metal signals increase steadily until the end of the 20$^{th}$ cycle. This implies that the formation of the dead Li metal in this system is not substantial during the initial cycles and is not the main reason for the initial capacity decay.

To further elucidate the process of capacity decay, we quantified $C_{dead}$ and $C_{SEI}$ for the entire cycles according to Eq. 2. The result shows that the $C_{dead}$ and $C_{SEI}$ gradually accumulate with prolonged cycling (Fig. 2C). During the initial three cycles (stage I), $C_{SEI}$ dominates the capacity loss, consuming 14.6 ± 5.7% (average value from three independent tests) of the overall capacity, while the number for dead Li metal is 5.8 ± 0.2% (Fig. 2E), which is in line with the observation of Grey and co-workers (*11*). Subsequently, at stage II, $C_{dead}$ increases gradually and reaches the same level as $C_{SEI}$ in eighth cycles. When the capacity decays to 0, x-ray diffraction (XRD) patterns show that the $LiFePO_4$ cathode has been fully delithiated to $FePO_4$ (fig. S5), indicating that all Li ions have been completely extracted from the cathode, which are then converted to "dead Li metal" and SEI species at the anode side (Fig. 2F). At this point, according to our quantitative results, $C_{dead}$ and $C_{SEI}$ consume 50.4 ± 5.1% and 47.3 ± 5.8% of the active capacity, respectively. Note that this result is obtained in the baseline electrolyte consisting of typical carbonate solvents, and the quantification suggests that the formation of dead Li metal and SEI, although occurring at different rates, both contribute relatively equally to the final capacity loss. In addition, we discovered that the newly formed dead Li metal is metastable and can self-dissolve in the electrolyte during the resting period. This

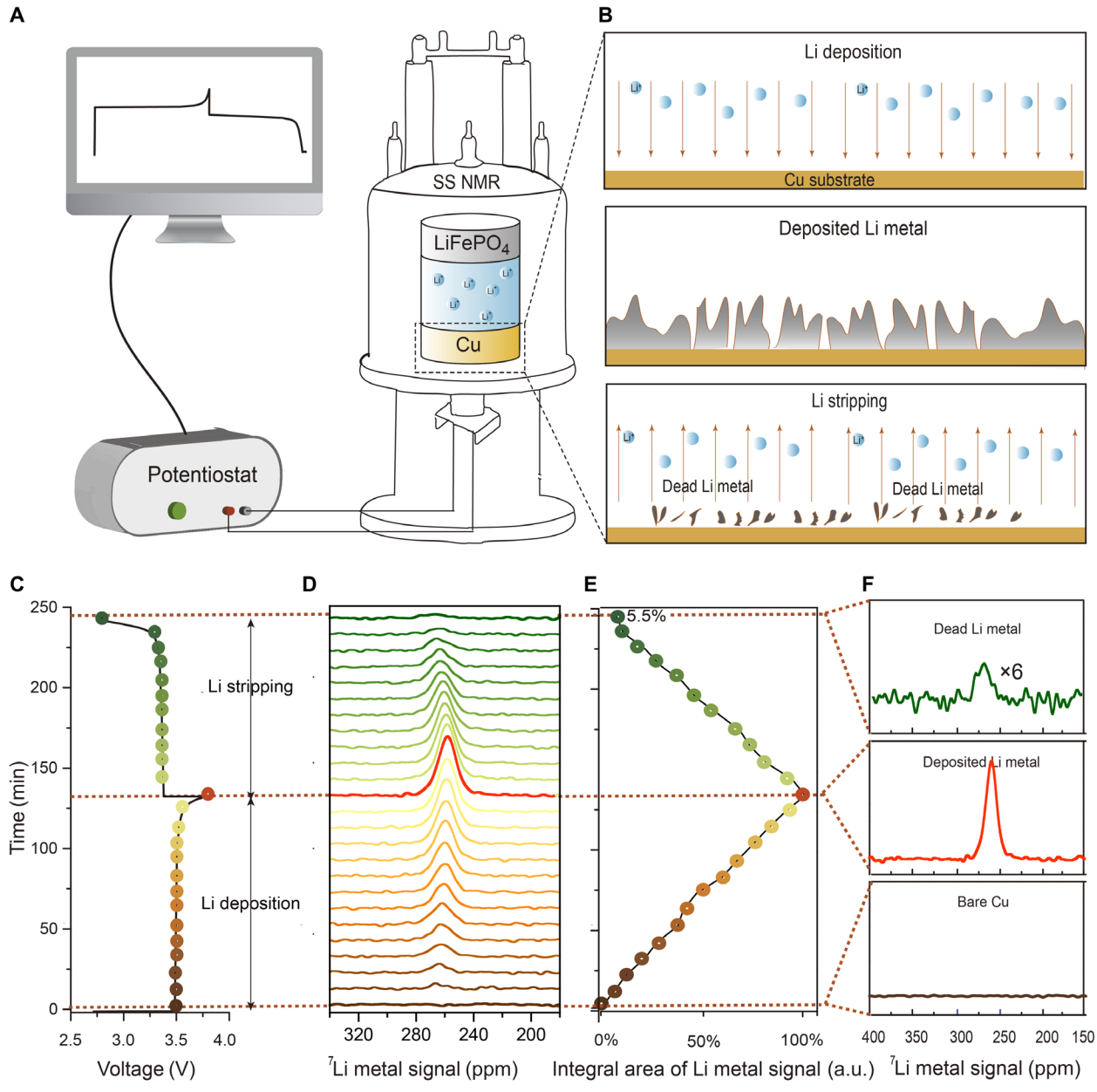


**Fig. 1. Schematics of the operando NMR study on the AFB using 1 M LiPF6/EC:EMC (3:7 by weight) electrolyte.** (**A**) Operando NMR setups. (**B**) Schematic of Li metal deposition/stripping on the Cu substrate in the Cu||$LiFePO_4$ battery. (**C**) The first charge (Li deposition) and discharge (Li stripping) cycle curves of operando Cu||$LiFePO_4$ cell and (**D**) the corresponding $^7$Li NMR spectra of the Li metal, and (**E**) their normalized integrals during charge and discharge process. (**F**) $^7$Li NMR spectra at the cell at open-circuit voltage (OCV), fully charged state, and fully discharged state. The integrals at the fully charged state and the fully discharged state are linked to the amount of deposited Li metal and the dead Li metal, respectively. a.u., arbitrary units.

**Table 1. Quantified distribution of dead Li metal and SEI with operando NMR in the baseline electrolytes at the first cycle.**

| | Electrochemistry measured | | | NMR measured | Calculated |
|---|---|---|---|---|---|
| | First charge | First discharge | Irreversible capacity | Dead Li metal | SEI |
| Capacity (μA·hour) | 286 | 259 | 27 | 15 | 12 |
| Normalized to the first charge capacity (a.u.) | 100% | 90.6% | 9.4% | 5.2% | 4.2% |

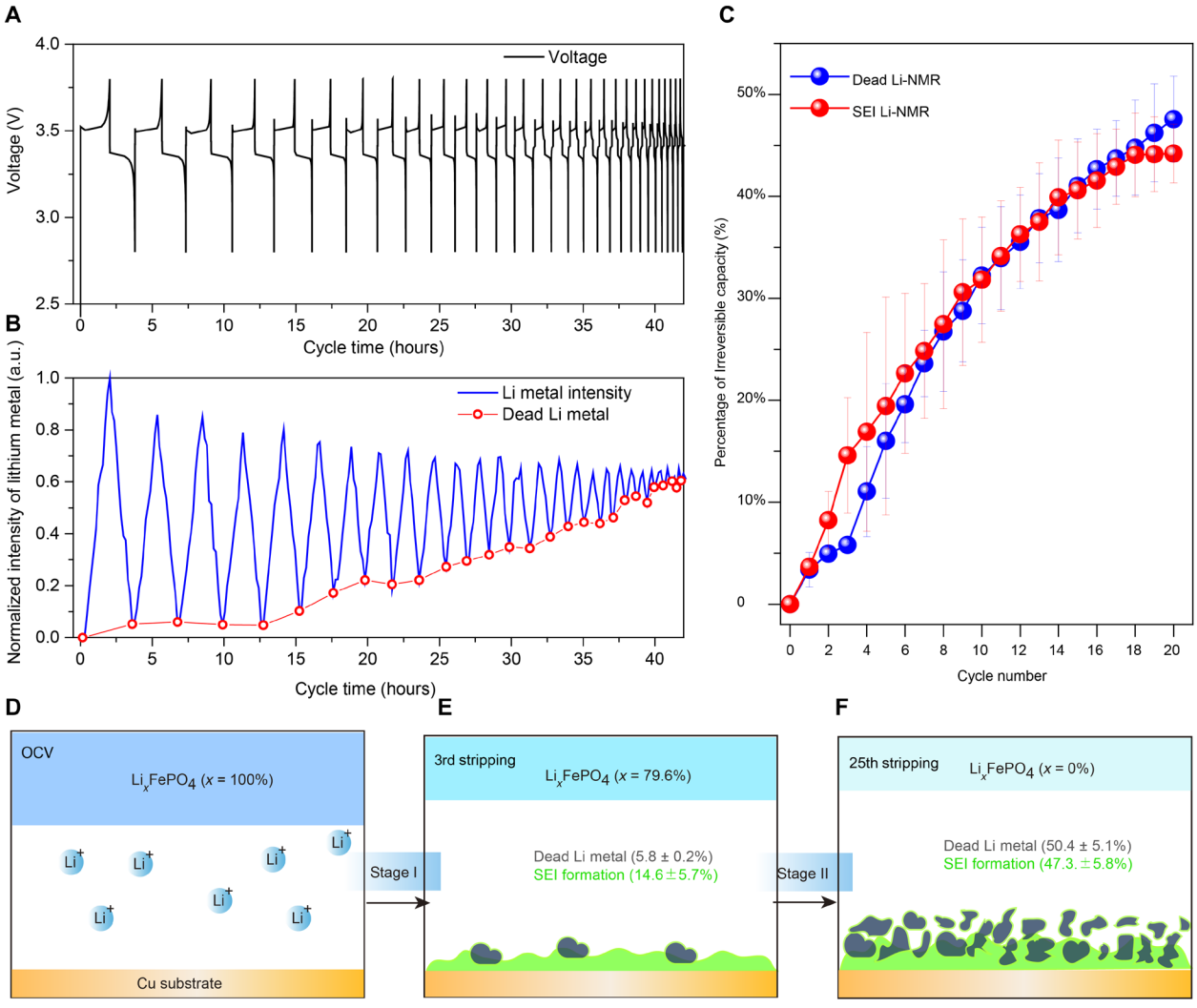


**Fig. 2. Operando $^7$Li NMR results of Cu||LiFePO$_4$ cell in 1 M LiPF$_6$/EC:EMC (3:7 by weight) electrolyte during cycling: From the first cycle until capacity decay to 0.** (**A**) Voltage–cycle time curves under 0.5 mA/cm$^2$ current density. (**B**) Evolution of the integral area of the detected Li metal signal with cycle time. The red dots are specified at the end of discharge state for each cycle, which represent the signals of dead Li metal. These signals of dead Li metal are converted into microampere·hour according to method explained in the Supplementary Text and then normalized by the first charge capacity (286 μA·hour), denoted as the $C_{dead}$ (%). The capacity loss caused by SEI ($C_{SEI}$) for each cycle is calculated by $C_{SEI}$ = irreversible capacity − $C_{dead}$. The error bars are from three independent NMR experiments. (**C**) The evolution of reversible capacity, $C_{dead}$ and $C_{SEI}$, which can be depicted into two stages according to the different growth rates of dead Li meal. A schematic of the two-stage process at the OCV period, and after the 3rd and 25th cycles at the discharged state is illustrated in (**D**) to (**F**).

dissolving process accelerates at elevated temperatures (fig. S6). Studying the unstable dead Li metal is always a challenge, and in situ/operando analytic technique has natural advantage for zero disturbance of these highly reactive species. Here, operando NMR technique can capture the highly reactive and transient species and provide quantitative information about the evolution of the dead Li metal and SEI, allowing us to clearly "visualize" the cell failure process.

## Quantitative reliability of dead Li by NMR

The quantitative capability of NMR has been discussed in the previous work (*12*, *13*) but rarely has it been mentioned when analyzing the metallic sample. As the total different failure mechanisms observed by NMR and TGC (*7*, *9*), it is important to compare the reliability of different quantitative techniques. Grey and co-workers suggest that the inconsistent failure mechanisms originate from different battery configurations. Here, to verify the reliability of quantitative results derived by different techniques, we complement our NMR study with ex situ TGC technique developed by Fang *et al.* (*7*), the details of which can be found in Materials and Methods. The dead Li metal is quantified by the amount of $H_2$ evolution on the basis of the following reaction: Li + $H_2O$➔LiOH + $H_2$. For the first cycle, TGC results show that the dead Li metal contributes to 3.1 ± 0.4% of irreversible capacity, which is comparable to our NMR results (3.7 ± 1.5%). Samples after prolonged cycles were selected for TGC analysis, and the accumulation of dead Li metal can be well depicted by the increasing area of $H_2$ in the gas chromatography (GC) data (fig. S7). Similar to NMR techniques, $C_{SEI}$ can be resolved in TGC analysis by

Eq. 2. A similar two-stage process was also observed in TGC results. In the later stages of cycling, $C_{dead}$ determined by TGC (denoted as $C_{dead}^{TGC}$) is obviously larger than that measured by NMR ($C_{dead}^{NMR}$) (Fig. 3A). To describe the similarity of results from the TGC and NMR measurements, we used the Euclidean distance defined in text S4 and found the value to be 27.1%, which indicates some noticeable difference in the quantification results from these two techniques (table S1).

We first exclude the influence of different battery configurations with different separators used in the NMR and TGC test. The TGC analysis was carried out for both operando cells and coin cells, presenting the consistent quantitative results of dead Li metal, indicating that the gap between NMR and TGC is not caused by different battery separators (fig. S9). Another possible source for such gap is the presence of LiH, which has been first proposed by Aurbach *et al.* (*14*), and then was observed at the surface of Li metal during plating by Kourkoutis and co-workers (*15*) using electron energy loss spectroscopy. Recently, the presence of LiH in inactive Li was further confirmed by both mass spectrometer titration (*16*, *17*) and synchrotron XRD (*18*) techniques. However, the influence of LiH on the accuracy of single TGC technique when quantifying dead lithium has not been compared and discussed yet, which is critical for evaluating the accuracy and applicability of a quantitatively analytical technique.

Here, we used a titration mass spectrometer (MST) with isotope-labeled $D_2O$ as the third quantitative method to study the existence of LiH, because $D_2O$ reacts with Li metal to form $D_2$ gas, while $D_2O$ reacts with LiH forming semi-heavy hydrogen (HD). The HD signal was observed in the inactive Li formed after the first cycle in AFBs (fig. S10), confirming the existence of LiH. That is to say, in the non-labeled TGC experiments, dead Li metal is not the sole source of $H_2$ formation. Note that the HD signal is also observed when analyzing inactive Na in Na metal batteries, and the presence of NaH in inactive Na has been verified by $^{23}$Na solid-state NMR (fig. S11). The dataset here suggests that the presence of alkali metal hydride and HD signal observed in MST are highly correlated. Moreover, the HD signal of inactive Li gradually increases with cycle number, indicating that LiH accumulates during cycling, and its irreversible formation may be responsible for capacity loss of Li metal (fig. S13).

To further study the influence of LiH on the quantification for dead Li metal, the amount of LiH and dead Li metal is estimated by the area under the HD and $D_2$ signals, respectively. The details of the quantification processes are given in text S3. The amount of dead Li metal ($C_{dead}^{MST}$) quantified by MST is comparable to that determined by NMR (Fig. 3A) with a similarity value (Euclidean distance) of 7.1% (table S1). The quantification results of LiH suggest that the formation of LiH increases slowly in the first eight cycles, and then, it is followed by a rapid increase (fig. S14B). Simultaneously, we notice an obvious deviation in $C_{dead}$ after eight cycles between the TGC and NMR/MST results (Fig. 3A). We correlate the amount of LiH with the difference in $C_{dead}$ determined by different techniques. $|C_{dead}(MST) - C_{dead}(NMR)|$ is independent from the increase in LiH, which can be explained by the inherent nature of the NMR and MST techniques that can avoid the interference of LiH. Nevertheless, $|C_{dead}(TGC) - C_{dead}(NMR)|$ and $|C_{dead}(TGC) - C_{dead}(MST)|$ show a positive correlation with the amount of LiH, suggesting that LiH is highly likely to be responsible for the deviation between the TGC and NMR/MST techniques when used for quantifying dead Li metal. Furthermore, on the basis of the amount of LiH determined by MST, we deduct the contribution of LiH in the TGC results, denoted as $C_{dead}$ (TGC-LiH correction). The process of deduction is described in detail in text S3. The TGC-LiH–corrected results show good similarity with $C_{dead}$(MS) and $C_{dead}$(NMR), with Euclidean distances to be 6.5 and 10.4%, respectively (fig. S15). The comparisons between the three techniques show the feasibility and reliability of NMR in quantifying the amount of inactive lithium. The deviation of the TGC results from the NMR/MST results also emphasizes the importance of considering the presence of LiH when quantifying Li metal in the battery systems, especially for analyzing batteries after extended cycling. Note that the amount of LiH formation is closely related to the electrolyte formulations and cycling histories. For example, we found that the formation of LiH can be suppressed by using fluoroethylene carbonate (FEC) additives (fig. S16), but its formation still increases with cycling, which

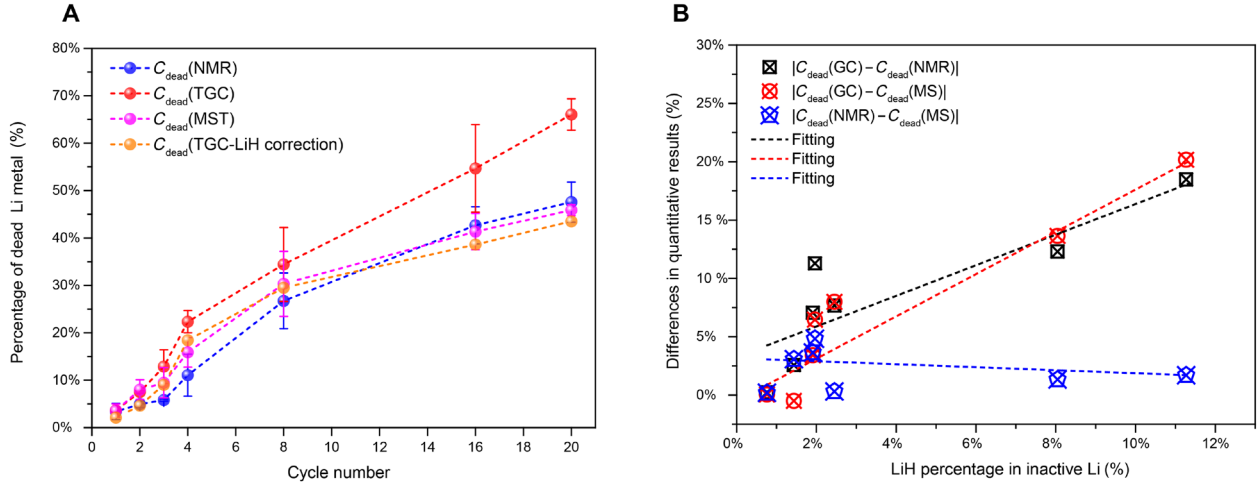


**Fig. 3. Quantitative reliability of the NMR method and the effects of LiH.** (**A**) The amount of dead Li metal quantified by NMR, TGC, MST, and corrected TGC techniques in baseline cells. In the corrected TGC analysis, the interference of LiH is excluded according to equations shown in text S3. (**B**) The relationship between the amount of LiH and the difference in quantitative results obtained by the three techniques.

brings uncertainties in quantifying dead Li metal. Because the lithium in LiH is in the ionic state, we ascribe it to the SEI species, similar to recent few reports on this topic (*17*, *18*). We believe the unambiguous identification of LiH implies important battery chemistry behind and needs further detailed study. Our present work focuses on the direct comparison of dead Li metal and SEI species. Therefore, LiH will be included in the SEI species for the following discussion.

### Effects of electrolyte and cycling conditions

The electrochemistry performance of LMBs is dictated by electrolyte formulations and the cycling condition. The formation of dead Li metal and SEI during the aforementioned conditions may vary. In this part, we evaluate the failure mechanisms under two different conditions: (i) in the presence of FEC as additive and (ii) cycling the cell at higher stripping rates (0.5 mA $cm^{-2}$ for deposition and 1.0 mA $cm^{-2}$ for stripping), hereafter denoted as AD cell and HD cell, respectively. These cells are compared to the baseline cell, which is operated with the baseline electrolyte and under moderate stripping rate (0.5 mA $cm^{-2}$ for deposition and 0.5 mA $cm^{-2}$ for stripping). In the first cycle, the signals of the dead Li metal can be observed in HD cell but not in AD cell (figs. S18A and S19A), demonstrating the capability of FEC in suppressing dead Li metal, which is in line with the MST and TGC results (fig. S17). The absence of the dead Li metal in AD cell can be ascribed to a highly fluorinated SEI derived from FEC (*19*). Figure 4 (A and B) shows their respective operando data for prolonged cycles. Despite the difference observed in the first cycle, all cells exhibit the continuous accumulation of dead Li metal during cycling, although the accumulation rates vary. The amount of dead Li metal in the AD cell increases slowly, while it increases sharply in the HD cell. The total amounts of dead Li metal at the end of the cycle for the three cells are different (dashed line in Fig. 4, A and B). On the basis of the operando data, we can quantitatively calculate the $C_{dead}$ and $C_{SEI}$ for the three cells and plotted the $C_{dead}$ versus $C_{SEI}$ curves to compare the amounts of dead Li metal and SEI in real time (Fig. 4C). Characteristically, all curves start from the zero point ($C_{dead}$ = 0 and $C_{SEI}$ = 0) and approach to the line of $C_{SEI}$ + $C_{dead}$ = 1 (blue dashed line). On the basis of the assumption that capacity loss only comes from dead Li metal and SEI, these curves can be interpreted as the competitive consumption between $C_{dead}$ and $C_{SEI}$ for the total active capacity. In addition, we divided Fig. 4C into two regions: SEI-dominated and dead Li metal–dominated regions, separated by the red line of $C_{dead}$ − $C_{SEI}$ = 0. The previous results shown in Fig. 2 for the baseline cell are also plotted in Fig. 4C as a reference. The baseline curve falls in the middle region at the end (50.4 and 47.3%), indicating nearly equal contributions of dead Li metal and SEI to the failure of Li metal. In contrast, the curve of FEC additive cell locates all within the SEI-dominated region during the entire cycling process, suggesting that the formation of SEI becomes the major culprit for the observed capacity decay. With a higher stripping current density, however, the capacity consumption by the dead Li metal increases significantly to 73.8 ± 4.6%, demonstrating that at high stripping current density, more dead Li metal are likely to form. The similar failure mechanism for each case is then verified by ex situ MST analysis (fig. S20), demonstrating the ability of NMR in quantifying inactive Li at different operating conditions and its ability to identify the different failure mechanisms of Li metal.

Scanning electron microscopy (SEM) was further used to investigate the morphology of inactive lithium at the end of cycling (Fig. 4, D to F). A fiber-like morphology, full of pulverized dead Li metal (Fig. 4D), is observed for the baseline cell. However, the SEM image of AD cell contains piled-up small particles rather than fibrous dead Li metal, the morphology of which is strongly related to the nature of the SEI (Fig. 4E). In contrast, more substantial dead Li metal is observed in the HD cell (Fig. 4F), which is not unexpected because dead Li metal causes 73.8 ± 4.6% capacity loss based on our quantitative analysis of the operando NMR data.

### Two-stage failure mechanism

We report that the two-stage failure mechanism of Li metal is a universal phenomenon for various operating conditions, as illustrated in Fig. 4C. The "T"-shaped profiles have been observed for all cases. In the initial cycles (stage I), all curves locate in the SEI-dominated region and dominantly grow along the axis of $C_{SEI}$, indicating that the increasing $C_{SEI}$ is the main reason of capacity loss during the initial cycles. The continuous formation of SEI can be attributed to the intrinsic instability of the organic electrolytes at low potential, leading to side reactions at the anode side. These side reactions become more severe for cells containing highly reactive additives (AD cell). In stage II, these curves start to grow along the axis of $C_{dead}$, suggesting an increase in dead Li metal formation in the subsequent cycles. We also noticed that only the SEI-dominated process was reported by Grey and co-workers. This can be rationalized by the limited cycle presented, where only the initial five cycles were discussed. This also highlights the importance of operando technique to dynamically monitor the whole process of inactive Li, and the failure mechanism would vary due to the different evolution rates of dead Li metal and SEI species.

The formation of the dead Li metal is highly correlated with the morphologies of the deposited Li (*5*, *7*). The mossy and/or dendritic Li deposits tend to form dead Li metal upon stripping, partially due to the uneven Li metal stripping process at kinks, and high stripping current density worsens such uneven dissolution (*20*). SEM was used to study the Li deposits in baseline electrolyte. The fourth deposition was selected for SEM measurement because, generally, thereafter there was a marked increase in the growth of dead Li metal, as shown in fig. S3B. However, the undisguisable morphologies of lithium metal and SEI make it difficult to investigate dead Li metal and SEI separately.

With operando NMR, we could infer the morphology evolution of the deposited Li metal and the dead Li metal on the basis of their $^7$Li chemical shifts. Because of the bulk susceptibility effect, the $^7$Li chemical shift of Li metal is affected by its surface microstructures (*10*). For example, the $^7$Li chemical shift of a dendritic lithium metal that is parallel to the external magnetic field ($B_0$) is centered at 275 ppm, while the chemical shift of a planar Li metal that is perpendicular to $B_0$ would appear at 240 ppm (Fig. 5, D and E) (*10*). Baseline and HD cells were selected to study the morphology evolutions as they use the same electrolyte (thus excluding the effect of SEI on the morphology change).

To illustrate the newly deposited Li microstructure, we plotted the difference spectra in Fig. 5 (A and B) as such: The $^7$Li NMR spectrum of the deposited Li metal at the $n^{th}$ ($n$ > 1) cycle is obtained by subtracting the $^7$Li NMR spectrum acquired at $(n\text{-}1)^{th}$ stripping state from the $^7$Li NMR spectrum acquired at $n^{th}$ deposition state. The resulting $^7$Li NMR spectra of the deposited Li metal in baseline electrolyte are presented in Fig. 5A and fig. S21, which can also be explained by a two-stage process. At stage I (initial four

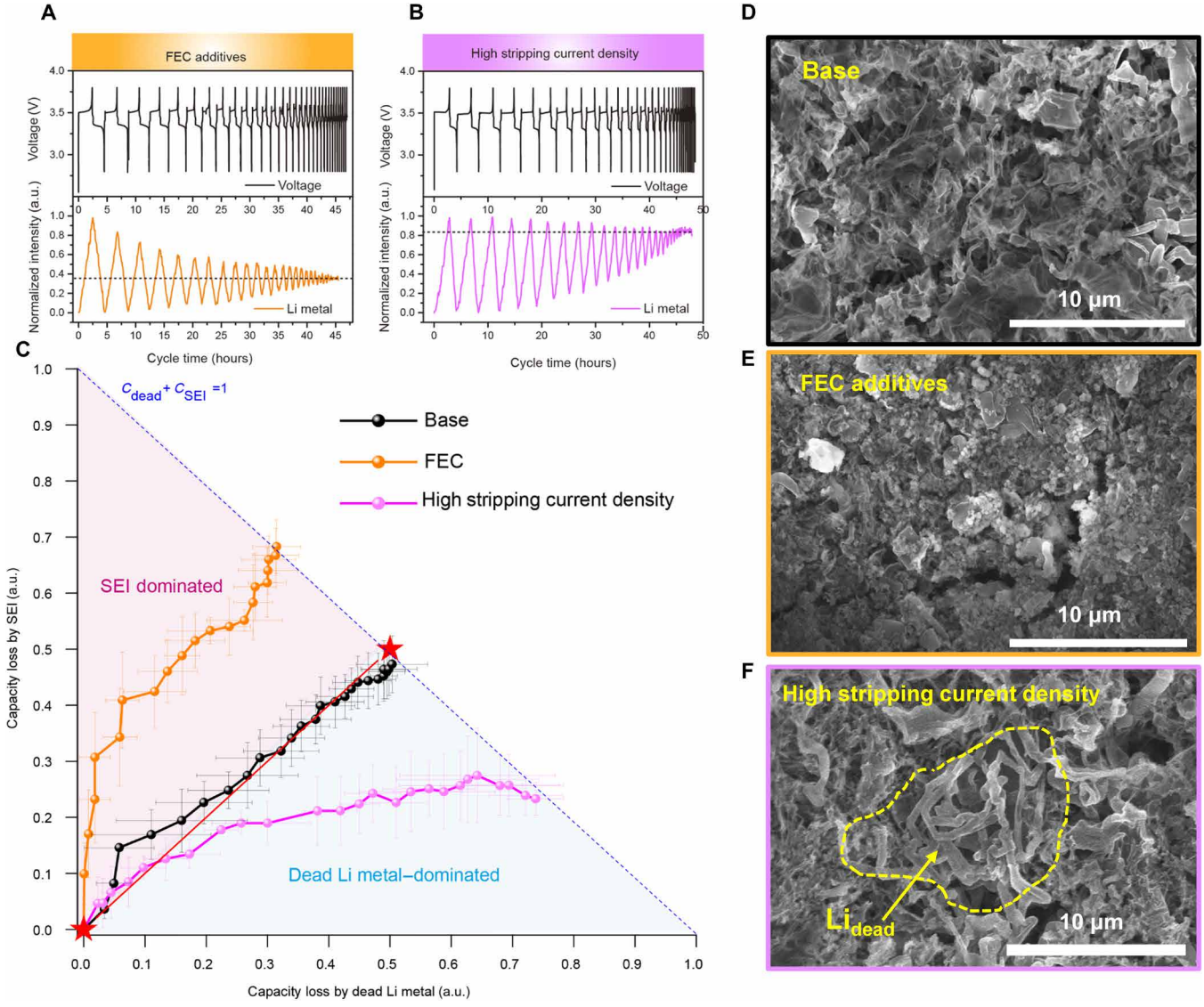


**Fig. 4. The impact of FEC additives and high stripping current density on the formation of dead Li metal and SEI.** Operando NMR data under different cycle conditions: (**A**) using FEC additive and (**B**) applying high stripping current (1.0 mA $cm^{-2}$). (**C**) The normalized capacity loss due to SEI formation ($C_{SEI}$) versus that due to the dead Li metal ($C_{dead}$) in baseline cell consisting of $LiFePO_4$||Cu cell (black line), FEC-containing cell (orange line), and high stripping current density cell (purple line). All curves start from the zero point ($C_{dead} = 0$ and $C_{SEI} = 0$) and approach to the line of $C_{SEI} + C_{dead} = 1$ (blue dashed line). Points on this line correspond to the relative value of $C_{SEI}$ and $C_{dead}$ as the batteries fail completely (capacity decay to 0). The SEI-dominated region and the dead Li metal–dominated region are separated by the line of $C_{SEI} = C_{dead}$ (red line). (**D** to **F**) SEM images of the inactive lithium on the anode substrate after complete cell failure.

cycles), a downfield shift toward 264 ppm (mossy lithium) is clearly observed, suggesting a structural change from smooth Li to mossy Li, deteriorating lithium metal morphology at this stage. During this process, the increase rate of $C_{dead}$ is slow. After that, the chemical shift remains at ~264 ppm, which corresponds to the typical mossy-type Li metal (*10*, *21*). Simultaneously, we observed a significant increase in $C_{dead}$ (Fig. 2C). By combining the NMR peak intensity and chemical shift analysis, a correlation between the morphology of Li deposits and the amount of dead Li metal can be established and quantified. Figure 5E presents a strong correlation between the downfield shifts of $^7$Li NMR signal of the Li deposits and the fast growth of dead Li metal.

Moreover, we observed that the larger the chemical shifts downfield during the first stage, the more dead Li metal forms at the second stage. For instance, a larger chemical shift from 258 to 270 ppm is found in HD cell during the initial 10 cycles (Fig. 5B), which implies that the Li metal deposits are mainly dendritic. As a result, more dead Li metal is generated at the end of the cycle (~70%) (Fig. 5E). The data suggest that the degree of Li morphology deterioration is related to the amount of dead lithium formed, as illustrated in Fig. 5E. It can be reasonably inferred that regulating the uniform deposition of lithium metal can potentially minimize the amount of dead lithium, which highlights the significance of controlling the morphology of lithium metal.

We observed a similar chemical shift for baseline cell and AD cell, but AD cell contains less dead lithium metal (fig. S22), which suggests the morphology of Li metal may not be the only reason that

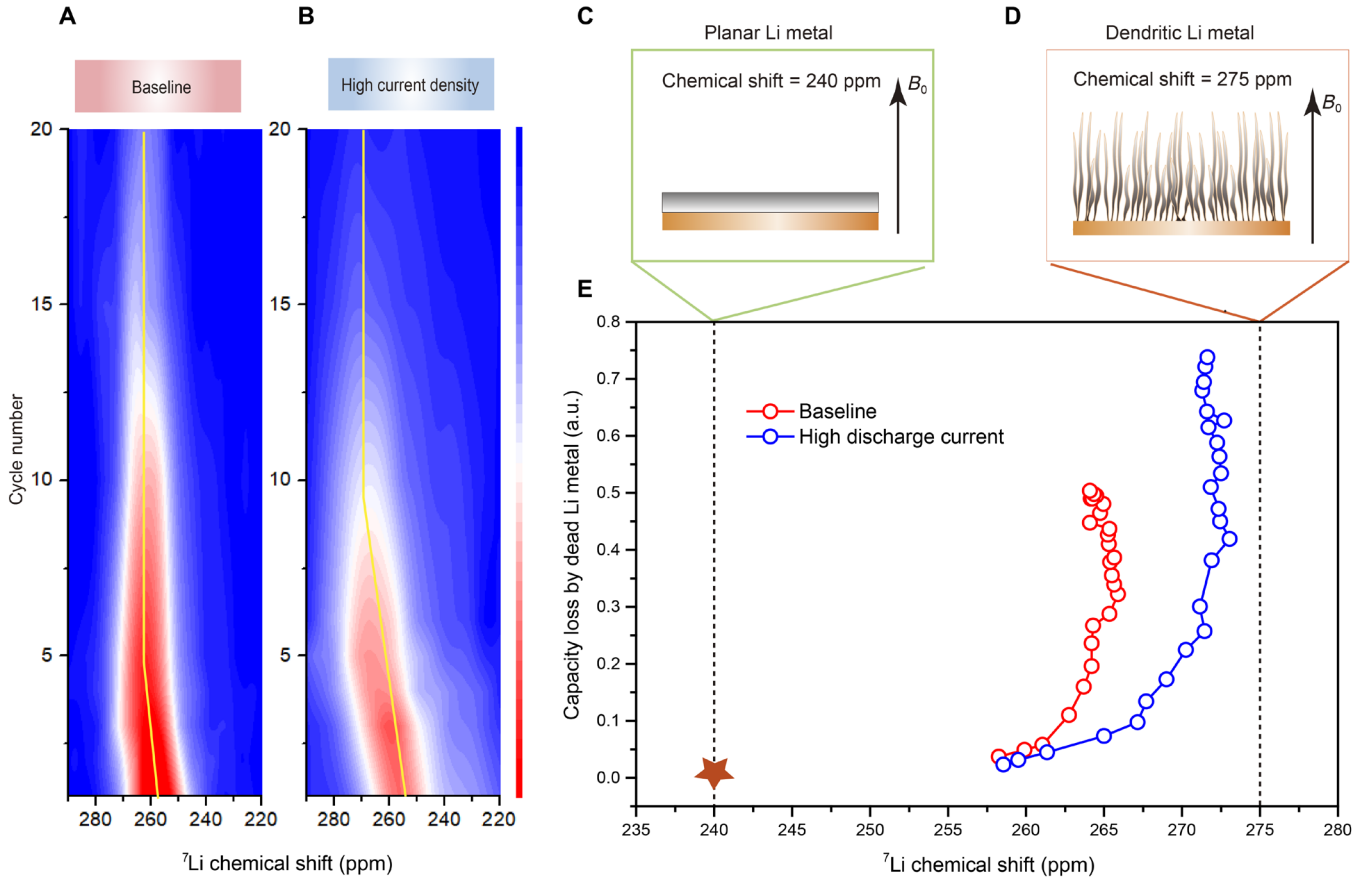


**Fig. 5. Correlation between deposited Li morphologies and the capacity loss by dead Li metal.** $^7$Li NMR spectra of newly deposited Li during each cycle as the function of cycle number in (**A**) baseline cell and (**B**) HD cell. The $^7$Li chemical shifts for different Li metal morphologies: (**C**) planar Li metal and (**D**) dendritic Li metal. (**E**) $^7$Li chemical shifts of Li deposits versus the capacity consumed by dead Li metal during deposition/stripping cycles. These data are the average value calculated on the basis of three tests.

determines the formation of dead Li metal. The additive FEC leads to an entirely different SEI compared with baseline electrolyte, whose properties including ionic conductivity, mechanic strength, and homogeneity also exert a large impact on the formation of dead Li metal, as revealed by studies conducted with cryo–electron microscopy (*22*).

## A performance-enhancing strategy and general failure scenario of Li metal

The two-stage failure mechanism for Li metal is related to the morphological deterioration of lithium deposits, from smooth deposition to dendritic Li as evidenced by the $^7$Li chemical shift change. Combined with previous results, we proposed that a performance-enhancing strategy should include (i) minimizing the SEI formation during the initial cycling, forming a thin SEI film that is ionic conducting, flexible, and has good adhesion with Li metal, and (ii) controlling the morphology of Li deposits as dense and uniform as possible in the second Li deposit stage, and in this case, amorphous Li deposit could be better than the crystalline one (*23*), because dense and uniform Li deposits are critical for delaying or suppressing the "dead Li metal formation" process.

Accordingly, we used an advanced electrolyte [2 M LiFSI + 2 M LiTFSI/DOL:DME + 2 weight % (wt %) $LiNO_3$] to test its ability in improving the cyclability of AFBs (*24*, *25*). The combination of high concentration lithium salt and ether solvent reduces the reactivity of the electrolyte solvent toward Li metal, thus forming a thin and stable SEI layer. The addition of lithium nitrate as an additive promotes the formation of spherical uniform Li deposits with optimized Li morphology (fig. S23) (*26*). Consequently, the capacity retention of in situ Cu||$LiFePO_4$ cell increases markedly from ~0% (baseline) to ~50% after 25 cycles (fig. S24). Impressively, operando NMR of this system shows negligible formation of dead lithium metal, even after 100-hour cycling (Fig. 6A), only exhibiting the SEI-dominated failure mechanism. After cycling in the advanced electrolyte, the optical images of the residue Li on Cu substrate are black, similar to the observation reported in other high-concentration electrolyte systems (*4*, *25*). This black residue Li species may be related to the formation of a high–ionic conductivity SEI (fig. S25A). In contrast, some dark gray residues are observed for samples cycled in baseline electrolyte, which is documented to be the dead Li metal covered by a thick SEI (fig. S25B) (*25*).

On the basis of the interpretation of the NMR results above, we propose three failure mechanisms and present the simulated operando NMR results for each case in Fig. 6. In the first mechanism, the Li metal degradation is mainly due to the SEI formation as shown in Fig. 6A. In this case, the dead lithium metal signal remains

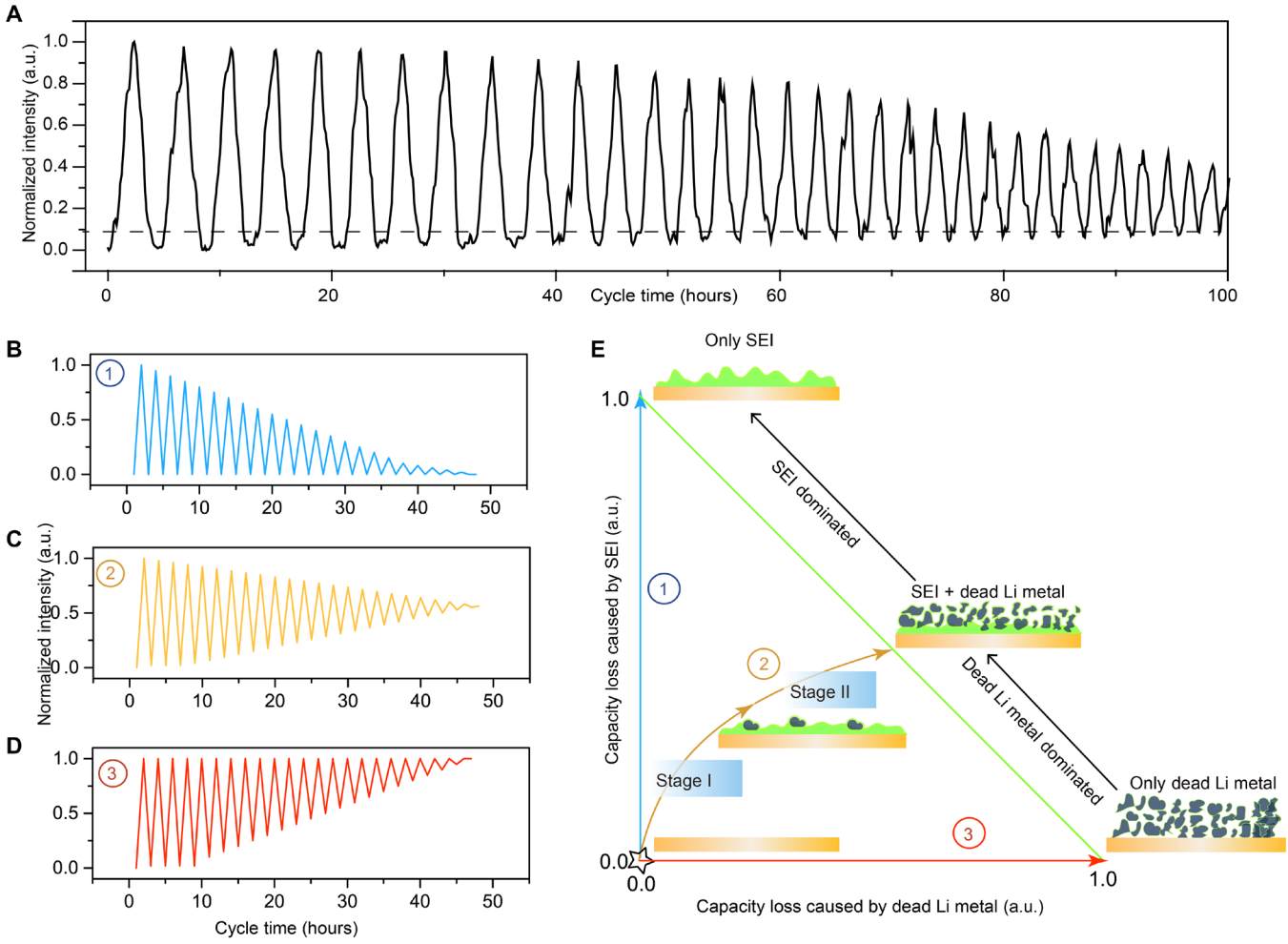


**Fig. 6. Enhancing strategies and schematic of typical failure mechanisms.** (**A**) The Li metal intensity varied with cycle time in the operando Cu||$LiFePO_4$ cell with advanced electrolyte. The simulated $^7$Li NMR intensity of lithium metal versus cycle time for three typical failure mechanisms: (**B**) SEI failure mechanism, (**C**) dead Li metal/SEI mixed failure mechanism, (**D**) dead Li metal mechanism, and (**E**) their corresponding $C_{dead}$ versus $C_{SEI}$ curves.

around zero, but the maximum of Li metal intensity decays with cycling time, indicating that the active lithium metal is continuously consumed to form other lithium-containing species such as Li-containing SEI. This is the case observed for AFB operating in high-performance electrolyte and in cells with FEC additive. The other extreme failure mechanism is the formation of dead lithium metal with negligible SEI formation, as illustrated in Fig. 6C. Theoretically, the maximum of Li metal intensity always equals to 1. This is because under this failure mechanism, both active lithium and inactive lithium are metallic lithium, so the total $^7$Li NMR signal of the lithium metal should remain unchanged. However, in reality, the capacity loss comes from both dead lithium metal and SEI. The last mechanism involves the simultaneous formation of dead lithium and SEI, and the corresponding simulated $^7$Li NMR signal of lithium metal signal is shown in Fig. 6B. This mechanism can be well depicted by two stages, indicating that the observed failure mechanism also depends on the cycle histories of LMBs. For instance, in the HD cell, the SEI formation dominates the capacity loss at the initial stage, but dead Li metal takes over in the following cycles and becomes the culprit of capacity loss.

## DISCUSSION

Our work first aims to establish a benchmark for quantifying inactive lithium, and three typical conditions were selected to demonstrate the diverse failure mechanisms, and we hope to inspire more comprehensive research on inactive lithium formation under specific cycling conditions, such as the effects of variation of charging/discharging current density (*27*), capacity usage (*5*, *28*), and temperature (*29*). Note that the methods presented here are not just limited to the Cu||$LiFePO_4$ batteries but can be extended to the high-voltage cathode, such as NCM and NCA, to further explore the cross-talk effects on the formation of dead Li (*30*, *31*). However, the degradation of cathode should be taken into consideration carefully as a source of capacity loss. Meanwhile, the other substrates with different surface chemistry (*32*) and geometry (*5*) have been reported to regulate the morphology of metal deposition, and their impacts on the formation of dead Li can also be further pursued in the future studies.

In summary, a comprehensive, quantitative, and in-depth investigation on Li metal deposition/stripping in an AFB has been performed using operando NMR spectroscopy. The reliabilities of the

quantification from NMR, TGC, and MST are rigorously compared, which proves that the deviation in quantitative results is due to the presence of LiH. The unambiguous identification of LiH suggests that the TGC method alone has limitations in quantifying dead Li metal. Meanwhile, it should be noted the capability of quantitative NMR is related to skin-depth effects and should be carefully used when the deposition area capacity is large (e.g., 4 mA·hour $cm^{-2}$ or about 20 μm for practical use). In this case, the ex situ MST is an alternative useful technique, although it is a destructive technique. Nevertheless, it can be expected that for some battery systems such as the solid-state batteries where the lithium metal/electrolyte interface is buried, destructive titration methods may be difficult to use precisely; thus, operando NMR should be a powerful tool to quantify inactive lithium during cycling. Overall, a series of combined approaches are indispensable to fully understand the complex failure modes of Li metal. These combined techniques will serve as useful tools in reevaluating the strategies used to relieve dead Li metal formation in LMBs and shed insight in designing advanced electrolyte materials for future research and development of practical LMBs. In addition, these techniques can be extended into other lithium metal–based systems, such as Li-sulfur, and solid-state Li batteries as well as the alkaline metal–based batteries, such as sodium counterparts.

## MATERIALS AND METHODS

### Electrochemical testing

$LiFePO_4$ cathode slurry was prepared by mixing 80 wt % LFP, 10 wt % polyvinylidene difluoride, and 10 wt % carbon black in *N*-methyl-2-pyrrolidone. The slurry was then cast on Al foil by a coating machine and dried in a vacuum oven at 80°C overnight with area mass loading of 1.25 ± 0.15 mA·hour $cm^{-2}$. The cathode film was punched into 14- and 6-mm disks for 2025 coin cells and operando cells, respectively. Cu||$LiFePO_4$ batteries were assembled using conventional 2025 coin cell in an Ar-filled glove box, bare Cu as anode substrates, and one layer of Celgard serving as the separator. Baseline electrolyte consists of 1 M $LiPF_6$ in EC/EMC(3:7 by weight), and FEC added electrolyte consists of 1 M $LiPF_6$ in EC/EMC (3:7 by weight) + 10% FEC. Advanced electrolyte consists of binary salts: 2 M LiFSI and 2 M LiTFSI dissolved in DOL:DME (1:1 by volume) + 2 wt % $LiNO_3$. All cells were cycled within voltage window between 2.8 and 3.8 V and with a fixed current density of 0.5 mA $cm^{-2}$, except the HD cell, which used 0.5 mA $cm^{-2}$ charge current density and 1.0 mA $cm^{-2}$ discharge current density. All electrochemical tests were performed on a LAND CT-20001A at 25°C.

### Characterization

The morphologies of the Li deposits and inactive Li were characterized by SEM (HITACHI S-4800) operated at 10.0 kV. Before the SEM test, all samples were washed by dimethyl carbonate three times and dried under vacuumed overnight. All samples were transferred in Ar for SEM analysis. The XRD patterns of $LiFePO_4$ were collected on a Rigaku Ultima IV power x-ray diffractometer equipped with Cu Kα radiation (λ = 1.5406 Å) at a scanning speed of 5° $min^{-1}$ in the 2θ range of 10° to 55°.

### Operando $^7$Li NMR

Operando $^7$Li NMR experiments were performed on a homemade in situ NMR probe head on a Bruker Avance 400 MHz spectrometer. The operando Cu||$LiFePO_4$ cells were assembled and sealed with wax in an argon glove box ($O_2$ < 0.5 ppm and $H_2O$ < 0.5 ppm). The details of operando NMR cells are shown in fig. S1, and the NMR setups are described in our previous work (*33*). To maintain the volume change of operando cell during cycling, two Celgard separators and one piece of glass fiber (Whatman) were used as separators (fig S1). Electrolyte (25 μl) was added in each cell. An NMR spectrometer was synchronized with the external electrochemical cycler, and a series of single pulse spectra were recorded with a small angle pulse of 6 μs, a sufficient delay of 1 s and 128 scans. The acquired series spectra were processed by Topspin package for automatic phase corrections and peak area integration. The detection limit of NMR in quantifying Li metal is at least 3.891 μg in this work (with 128 scans), which is discussed in detail in text S6.

### Titration gas chromatography

GC experiments were performed on a Shimadzu GC-2010 Plus Tracera. The experimental procedures were followed according to the previous work (*7*). The calibration curve was obtained by plotting the mass of pure Li metal (determined by high precision balance, $d$ = 0.001 mg) with the corresponding $H_2$ area measured by GC. The validation of the calibration curve was determined by comparing the mass of Li metal acquired by weighing and GC, respectively. For analyzing the inactive Li, the cycled $LiFePO_4$||Cu cells were disassembled in glove box ($H_2O$ < 0.5 ppm and $O_2$ < 0.5 ppm). Cu foil and separator were put into a 5-ml headspace vessel and sealed before taking out the glove box. Deionized water (0.1 ml) was injected into the headspace vessel. After the reaction is complete, an airtight syringe (10 μl) was pierced through the septum to extract 6 μl of reacted gas, which was then injected into the GC spectrometer. The obtained $H_2$ area was converted into the mass of dead Li metal and the corresponding capacity loss. The capacity loss caused by SEI is then calculated by the following equation: capacity loss by SEI = total capacity loss determined by electrochemistry − capacity loss caused by dead Li metal.

### Mass spectrometry titration

MST experiments were performed on a mass spectrometer (Hiden Analytical Ltd.). Similar to TGC analysis, Cu foil and separator were placed in a 5-ml headspace vessel and sealed before taking out the glove box. Two capillaries were quickly inserted into the headspace vessel: one with flushing argon gas (99.999%) and the other as outlet. After being filled with Ar, both capillaries were sealed with wax. Then, the vessel was connected to the mass spectrometer. After the ion current was stabilized, $D_2O$ (99.9%) was injected into the headspace vessel to react with inactive Li. The continuous flowing argon gas flushed the reaction gases in the headspace vessel to the mass spectrometer for analysis. Multiple-ion mode was used to record the ion current of mass/charge ratio ($m/z$) = 3 (for HD) and $m/z$ = 4 (for $D_2$). After these signals fully attenuated, we integrated the signal of HD and $D_2$ and converted it into the mass of dead Li metal and LiH through a preestablished calibration curve. The mass of dead Li metal and LiH was converted into the corresponding capacity loss on the basis of the following one-electron reactions: $Li^+ - e^{-1} \rightarrow Li^0$ and $Li^0 + 1/2H_2 \rightarrow LiH$.

## SUPPLEMENTARY MATERIALS

Supplementary material for this article is available at https://science.org/doi/10.1126/sciadv.abj3423

## REFERENCES AND NOTES


1. J. Liu, Z. Bao, Y. Cui, E. J. Dufek, J. B. Goodenough, P. Khalifah, Q. Li, B. Y. Liaw, P. Liu, A. Manthiram, Y. S. Meng, V. R. Subramanian, M. F. Toney, V. V. Viswanathan, M. S. Whittingham, J. Xiao, W. Xu, J. Yang, X.-Q. Yang, J.-G. Zhang, Pathways for practical high-energy long-cycling lithium metal batteries. *Nat. Energy* **4**, 180–186 (2019).
2. J. Zheng, M. S. Kim, Z. Tu, S. Choudhury, T. Tang, L. A. Archer, Regulating electrodeposition morphology of lithium: Towards commercially relevant secondary Li metal batteries. *Chem. Soc. Rev.* **49**, 2701–2750 (2020).
3. J. Xiao, Q. Li, Y. Bi, M. Cai, B. Dunn, T. Glossmann, J. Liu, T. Osaka, R. Sugiura, B. Wu, J. Yang, J.-G. Zhang, M. S. Whittingham, Understanding and applying coulombic efficiency in lithium metal batteries. *Nat. Energy* **5**, 561–568 (2020).
4. S. Chen, J. Zheng, D. Mei, K. S. Han, M. H. Engelhard, W. Zhao, W. Xu, J. Liu, J.-G. Zhang, High-voltage lithium-metal batteries enabled by localized high-concentration electrolytes. *Adv. Mater.* **30**, 1706102 (2018).
5. J. Zheng, T. Tang, Q. Zhao, X. Liu, Y. Deng, L. A. Archer, Physical orphaning versus chemical instability: Is dendritic electrodeposition of Li fatal? *ACS Energy Lett.* **4**, 1349–1355 (2019).
6. N.-W. Li, Y.-X. Yin, C.-P. Yang, Y.-G. Guo, An artificial solid electrolyte interphase layer for stable lithium metal anodes. *Adv. Mater.* **28**, 1853–1858 (2016).
7. C. Fang, J. Li, M. Zhang, Y. Zhang, F. Yang, J. Z. Lee, M.-H. Lee, J. Alvarado, M. A. Schroeder, Y. Yang, B. Lu, N. Williams, M. Ceja, L. Yang, M. Cai, J. Gu, K. Xu, X. Wang, Y. S. Meng, Quantifying inactive lithium in lithium metal batteries. *Nature* **572**, 511–515 (2019).
8. Y.-C. Hsieh, M. Leißing, S. Nowak, B.-J. Hwang, M. Winter, G. Brunklaus, Quantification of dead lithium via in situ nuclear magnetic resonance spectroscopy. *Cell Reports Phys. Sci.* **1**, 100139 (2020).
9. A. B. Gunnarsdóttir, C. V. Amanchukwu, S. Menkin, C. P. Grey, Noninvasive in situ NMR study of "dead lithium" formation and lithium corrosion in full-cell lithium metal batteries. *J. Am. Chem. Soc.* **142**, 20814–20827 (2020).
10. R. Bhattacharyya, B. Key, H. Chen, A. S. Best, A. F. Hollenkamp, C. P. Grey, In situ NMR observation of the formation of metallic lithium microstructures in lithium batteries. *Nat. Mater.* **9**, 504–510 (2010).
11. O. Pecher, J. Carretero-González, K. J. Griffith, C. P. Grey, Materials' methods: NMR in battery research. *Chem. Mater.* **29**, 213–242 (2016).
12. F. Malz, H. Jancke, Validation of quantitative NMR. *J. Pharm. Biomed. Anal.* **38**, 813–823 (2005).
13. P. Giraudeau, Challenges and perspectives in quantitative NMR. *Magn. Reson. Chem.* **55**, 61–69 (2017).
14. D. Aurbach, I. Weissman, On the possibility of LiH formation on Li surfaces in wet electrolyte solutions. *Electrochem. Commun.* **1**, 324–331 (1999).
15. M. J. Zachman, Z. Tu, S. Choudhury, L. A. Archer, L. F. Kourkoutis, Cryo-STEM mapping of solid–liquid interfaces and dendrites in lithium-metal batteries. *Nature* **560**, 345–349 (2018).
16. C. Gong, S. D. Pu, X. Gao, S. Yang, J. Liu, Z. Ning, G. J. Rees, I. Capone, L. Pi, B. Liu, G. O. Hartley, J. Fawdon, J. Luo, M. Pasta, C. R. M. Grovenor, P. G. Bruce, A. W. Robertson, Revealing the role of fluoride-rich battery electrode interphases by operando transmission electron microscopy. *Adv. Energy Mater.* **11**, 2003118 (2021).
17. G. Xu, J. Li, C. Wang, X. Du, D. Lu, B. Xie, X. Wang, C. Lu, H. Liu, S. Dong, G. Cui, L. Chen, The formation/decomposition equilibrium of LiH and its contribution on anode failure in practical lithium metal batteries. *Angew. Chem. Int. Ed.* **60**, 7770–7776 (2021).
18. Z. Shadike, H. Lee, O. Borodin, X. Cao, X. Fan, X. Wang, R. Lin, S.-M. Bak, S. Ghose, K. Xu, C. Wang, J. Liu, J. Xiao, X.-Q. Yang, E. Hu, Identification of LiH and nanocrystalline LiF in the solid–electrolyte interphase of lithium metal anodes. *Nat. Nanotechnol.* **16**, 549–554 (2021).
19. X.-Q. Zhang, X.-B. Cheng, X. Chen, C. Yan, Q. Zhang, Fluoroethylene carbonate additives to render uniform Li deposits in lithium metal batteries. *Adv. Funct. Mater.* **27**, 1605989 (2017).
20. K. N. Wood, E. Kazyak, A. F. Chadwick, K. H. Chen, J. G. Zhang, K. Thornton, N. P. Dasgupta, Dendrites and pits: Untangling the complex behavior of lithium metal anodes through operando video microscopy. *ACS Cent. Sci.* **2**, 790–801 (2016).
21. H. J. Chang, N. M. Trease, A. J. Ilott, D. Zeng, L.-S. Du, A. Jerschow, C. P. Grey, Investigating Li microstructure formation on Li anodes for lithium batteries by in situ $^{6}$Li/$^{7}$Li NMR and SEM. *J. Phys. Chem. C* **119**, 16443–16451 (2015).
22. Y. Li, W. Huang, Y. Li, A. Pei, D. T. Boyle, Y. Cui, Correlating structure and function of battery interphases at atomic resolution using cryoelectron microscopy. *Joule* **2**, 2167–2177 (2018).
23. X. Wang, G. Pawar, Y. Li, X. Ren, M. Zhang, B. Lu, A. Banerjee, P. Liu, E. J. Dufek, J.-G. Zhang, J. Xiao, J. Liu, Y. S. Meng, B. Liaw, Glassy Li metal anode for high-performance rechargeable Li batteries. *Nat. Mater.* **19**, 1339–1345 (2020).
24. F. Qiu, X. Li, H. Deng, D. Wang, X. Mu, P. He, H. Zhou, A concentrated ternary-salts electrolyte for high reversible Li metal battery with slight excess Li. *Adv. Energy Mater.* **9**, 1803372 (2019).
25. J. Qian, W. A. Henderson, W. Xu, P. Bhattacharya, M. Engelhard, O. Borodin, J.-G. Zhang, High rate and stable cycling of lithium metal anode. *Nat. Commun.* **6**, 6362 (2015).
26. Y. Liu, D. Lin, Y. Li, G. Chen, A. Pei, O. Nix, Y. Li, Y. Cui, Solubility-mediated sustained release enabling nitrate additive in carbonate electrolytes for stable lithium metal anode. *Nat. Commun.* **9**, 3656 (2018).
27. Y. Xu, H. Wu, H. Jia, J.-G. Zhang, W. Xu, C. Wang, Current density regulated atomic to nanoscale process on Li deposition and solid electrolyte interphase revealed by cryogenic transmission electron microscopy. *ACS Nano* **14**, 8766–8775 (2020).
28. S. Jiao, J. Zheng, Q. Li, X. Li, M. H. Engelhard, R. Cao, J.-G. Zhang, W. Xu, Behavior of lithium metal anodes under various capacity utilization and high current density in lithium metal batteries. *Joule* **2**, 110–124 (2018).
29. J. Wang, W. Huang, A. Pei, Y. Li, F. Shi, X. Yu, Y. Cui, Improving cyclability of Li metal batteries at elevated temperatures and its origin revealed by cryo-electron microscopy. *Nat. Energy* **4**, 664–670 (2019).
30. J. Betz, J.-P. Brinkmann, R. Nölle, C. Lürenbaum, M. Kolek, M. C. Stan, M. Winter, T. Placke, Cross talk between transition metal cathode and Li metal anode: Unraveling its influence on the deposition/dissolution behavior and morphology of lithium. *Adv. Energy Mater.* **9**, 1900574 (2019).
31. R. A. Vilá, W. Huang, Y. Cui, Nickel impurities in the solid-electrolyte interphase of lithium-metal anodes revealed by cryogenic electron microscopy. *Cell Reports Phys. Sci.* **1**, 100188 (2020).
32. Y. Gao, T. Rojas, K. Wang, S. Liu, D. Wang, T. Chen, H. Wang, A. T. Ngo, D. Wang, Low-temperature and high-rate-charging lithium metal batteries enabled by an electrochemically active monolayer-regulated interface. *Nat. Energy* **5**, 534–542 (2020).
33. Y. Xiang, G. Zheng, Z. Liang, Y. Jin, X. Liu, S. Chen, K. Zhou, J. Zhu, M. Lin, H. He, J. Wan, S. Yu, G. Zhong, R. Fu, Y. Li, Y. Yang, Visualizing the growth process of sodium microstructures in sodium batteries by in-situ $^{23}$Na MRI and NMR spectroscopy. *Nat. Nanotechnol.* **15**, 883–890 (2020).
34. E. J. McShane, A. M. Colclasure, D. E. Brown, Z. M. Konz, K. Smith, B. D. McCloskey, Quantification of inactive lithium and solid–electrolyte interphase species on graphite electrodes after fast charging. *ACS Energy Lett.* **5**, 2045–2051 (2020).



**Acknowledgments**

**Funding:** This research was financially supported by the National Key Research and Development Program of China (grant nos. 2018YFB0905400 and 2016YFB0901500) and the National Natural Science Foundation of China (grant nos. 21935009, 21761132030, and 21603231). We thank S. S. Yu for the technical support of the NMR experiments and D. Chen (University of British Columbia, Canada) for the discussion of MS data analysis. R.F. thanks the support from the National High Magnetic Field Laboratory, which is supported by NSF Cooperative Agreement NSF/DMR-1644779 and the State of Florida. K.X. also acknowledges the support from DOE Basic Energy Science via the Joint Center of Energy Storage Research (JCESR) under IAA SN2020957. **Author contributions:** Y.Y. and Y.X. planned the project. Y.Y. supervised the project. Y.X., Z.L., and M.T. carried out the NMR measurement. Y.X., M.T., and G.Zho. prepared the operando cells. Y.X. and M.T. performed the SEM measurements. Y.X., M.T., and N.X. performed the TGC experiments. Y.X., M.T., and X.H. performed the MST experiments. G.Zho. and R.F. provided technical support for in situ NMR. G.Zhe., X.L., and R.F. assisted in NMR data analysis. M.A., J.-G.Z., and K.X. participated in discussing the results and commenting on the manuscript. The manuscript was mainly written and revised by Y.X., G.Zho., Y.J., and Y.Y. All authors approved and revised the final version of the manuscript. **Competing interests:** The authors declare that they have no competing interests. **Data and materials availability:** All data needed to evaluate the conclusions in the paper are present in the paper and/or the Supplementary Materials.

Submitted 20 May 2021
Accepted 21 September 2021
Published 10 November 2021
10.1126/sciadv.abj3423